Nanocrystal-SnO₂-Loaded Graphene with Improved Li-Storage Properties Prepared by a Facile One-Pot Hydrothermal Route

Jian Xie, Shuang-Yu Liu, Xue-Fei Chen, Yun-Xiao Zheng, Wen-Tao Song, Gao-Shao Cao, Tie-Jun Zhu, and Xin-Bing Zhao[*]

Department of Materials Science and Engineering, Zhejiang University, Hangzhou 310027, China
[*]E-mail: zhaoxb@zju.edu.cn

Nanpcrystal-SnO2-loaded graphene was synthesized by a facile in situ one-pot hydrothermal route. The effects of tin sources (Sn2+ or Sn4+) and graphene on the morphology and electrochemical properties of SnO2 have been investigated. It was found that the graphite oxide plays a critical role in the oxidation of Sn2+ to Sn4+, and that SnO instead of SnO2 forms without adding the graphite oxide. SnO2 exhibits a smaller size (below 10 nm) and a more homogeneous dispersion on graphene using Sn2+ as the precursor compared with the case using Sn4+ as the precursor. The electrochemical tests showed that the SnO2-graphene nanocomposites exhibit obvious improved electrochemical properties compared to bare SnO2 due to the buffering, confining and conducting effects of the introduced graphene. We also found that the nanocomposite using Sn2+ as the precursor shows a better cycling stability than that using Sn4+ as the precursor.

Keywords: SnO2, graphene, nanocomposite, Li-storage properties, anode

1. INTRODUCTION

Since first reported by Idota et al. in 1997 that tin-based amorphous oxide could yield a high, stable capacity over 600 mAh g^{-1} [1], great efforts have been made to develop SnO₂-based anode materials for Li-ion batteries. The theoretical capacity of SnO₂ can reach as high as 780 mAh g^{-1} with a Li-storage mechanism as: $SnO_2 + 4Li \rightarrow Sn + 2Li_2O$, $Sn + xLi \leftrightarrow Li_xSn$ (x ≤ 4.4) [2]. This material, however, suffers from a rapid capacity fade due to the large volume changes (358%) during the Li-insertion/extraction processes of Sn. The research on a single SnO₂ nanowire using an in situ technique showed that the large volume changes do occur during the Li-insertion process [3, 4].

Many strategies have been taken to alleviate the volume changes for SnO₂. One of the effective methods is to use nanostructured materials. As reported by Kim et al., the SnO₂ exhibited a rather

stable cycling when its particle size was decreased to 3 nm [5]. Nanoparticles, however, tend to aggregate upon repeated cycling. A useful measure to overcome this problem is to load the nanoparticles onto a matrix. Carbon-based materials have been considered as the best choice as matrices because they not only increase the electrical conductivity but also contribute to the overall capacity, in addition to the buffering and dispersing effects. Up to now, various forms of carbon, such as amorphous carbon [6–9], graphite [10–12], and carbon nanotubes [13–15] have been proposed as the matrices to support the SnO_2 particles.

In recent years, graphene, a new two-dimensional carbon material, has attracted a considerable interest since first reported by Novoselov et al. [16]. Graphene is also considered as an ideal matrix to support the nanoparticles due to its appealing merits such as large specific surface area [17], high electronic conductivity [18], and high mechanical strength [19]. Previous work has shown that the electrochemical properties of SnO_2 can be remarkably improved by loading it onto graphene [20–25]. In these researches, SnO_2 was obtained using $SnCl_2 \cdot 2H_2O$ as the tin source in an open system [21–25]. The dissolved O_2 in the solution may serve as the oxidant to convert Sn^{2+} into Sn^{4+} in the open system. Herein, we report the preparation of a SnO_2-graphene nanocomposite using $SnCl_2 \cdot 2H_2O$ as the tin source in a sealed system. In this synthesis, the graphite oxide played a critical role in the oxidation of Sn^{2+} to Sn^{4+}. The direct proof is that SnO instead of SnO_2 forms without adding the graphite oxide. The effects of different tin sources (Sn^{2+} or Sn^{4+}) and graphene on the morphology and electrochemical properties of SnO_2 will be investigated in this work.

2. EXPERIMENTAL SECTION

2.1 Preparation of SnO₂/graphene

Graphite oxide (120 mg), which was prepared by the modified Hummer's method [26], was added into 60 mL of deionized (DI) water with sonication for 3 h to form a uniform dispersion. Then, 3 mmol of $SnCl_2 \cdot 2H_2O$ and 3 mmol of sodium citrate were added to the above dispersion with pH adjusted to 11 using ammonia water (25 % wt). The mixed solution was transferred to a Teflon-lined stainless steel autoclave (100 mL) and heated in an electric oven at 180 ºC for 4 h. The resulting product was separated by centrifugation, washed with DI water and dried at 60 ºC under vacuum for 8 h. The product is named SnO_2/G. A control experiment was also performed using the same route without adding graphite oxide (the product is SnO). The hydrothermal reactions were also carried out in hydrazine hydrate (HH, 85 % wt) and H_2O/HH (1:1 in volume) using $SnCl_2 \cdot 2H_2O$ as the tin source (with graphite oxide) by a similar procedure. For comparison, $SnCl_4 \cdot 5H_2O$ was also used as the tin source to synthesize bare SnO_2 and SnO_2-loaded graphene (named as SnO_2/G2) with the same route. All of the solutions were purged with Ar to remove O_2 before the hydrothermal reactions.

2.2 Materials Characterization

The crystalline phases of the obtained products were identified by X-ray diffraction (XRD) on a Rigaku D/Max-2550pc powder diffractometer equipped with Cu K_α radiation ($\lambda = 1.541$ Å). The

Raman spectra were recorded on a Labor Raman HR-800 (514.5 nm). X-ray photoelectron spectroscopy (XPS) were collected on a KRATOS AXIS ULTRA-DLD spectrometer with a monochromatic Al K_{α} radiation (hv = 1486.6 eV). The morphologies of the products were characterized by field emission scanning electron microscopy (FE-SEM, FEI-sirion), transmission electron microscopy (TEM, JEM 2100F) and high-resolution TEM (HRTEM, JEM 2100F). N_2 absorption/desorption isotherms were recorded on an AUTOSORB-1-C apparatus. Thermogravimetric analysis (TGA) was conducted on a DSCQ1000 instrument from 45 to 650 ºC at a ramp rate of 10 ºC min^{-1} in air.

2.3 Electrochemical measurements

The electrochemical properties of the hydrothermal products (SnO_2/G, SnO_2/G2, and SnO_2) were measured using CR2025-type coin cells. The hydrothermal product, polyvinylidene fluoride (PVDF) and acetylene black (75:15:10 in weight) were mixed in N-methyl pyrrolidone (NMP) and magnetically stirred for 2 h to make a slurry. The working electrodes were made by spreading the slurry onto Ni foam and dried at 100 °C under vacuum for 8 h. Cell assembly was carried out in an Ar-filled glove box using Li foil as the counter electrode and polypropylene microporous film (Celgard 2300) as the separator. The electrolyte used was 1 M LiPF$_6$ in ethylene carbonate (EC)/dimethyl carbonate (DMC) (1:1 by volume). The cells were charged and discharged galvanostatically on a Neware BTS-5V10mA battery cycler (Shenzhen, China) at 0.05-2 V (vs. Li/Li$^+$). Cyclic voltammetry (CV) tests were conducted on an Arbin BT2000 system between 0.05 and 2.0 V (vs. Li/Li$^+$) at 0.1 mV s^{-1}. Electrochemical impedance spectroscopy (EIS) measurements were conducted on a CHI660C electrochemistry workstation by applying an ac voltage of 5 mV amplitude in the frequency range from 10^{-2} to 10^5 Hz at de-lithiated states. All of the electrochemical measurements were carried out at room temperature.

3. RESULTS AND DISCUSSION

Fig. 1(a) shows the XRD patterns of the hydrothermal products prepared at 180°C for 4 h using $SnCl_2 \cdot 2H_2O$ as the precursor in DI water. The dominant diffraction peaks can be indexed to tetragonal SnO (space group *P4/nmm*, JCPDS No. 85-0423) when the graphite oxide was not added. The formation of minor SnO_2 was caused by the trace amounts of the dissolved O_2. In contrast, single-phase SnO_2 (space group *P4$_2$/mnm*, JCPDS No. 77-0452) forms in the presence of the graphite oxide. It is clear that the graphite oxide plays a critical role in the formation of SnO_2 by oxidizing Sn^{2+} to Sn^{4+}. Fig. 1(b) shows the XRD patterns of the products under the reducing condition (with HH). HH is generally used to reduce graphite oxide to graphene in the solution route [27]. SnO could form using Sn^{2+} as the tin source and HH as the solvent in a sealed system [28]. In this work, however, SnO_2 still dominates the products under the reducing environment in the close system, indicating that the graphite oxide could oxidize Sn^{2+} to Sn^{4+} before it was reduced to graphene. Fig. 1(c) gives the XRD

patterns of the hydrothermal products using SnCl$_4$·5H$_2$O as the tin source. As expected, the reaction products are SnO$_2$, no mater whether the graphite oxide was added or not.
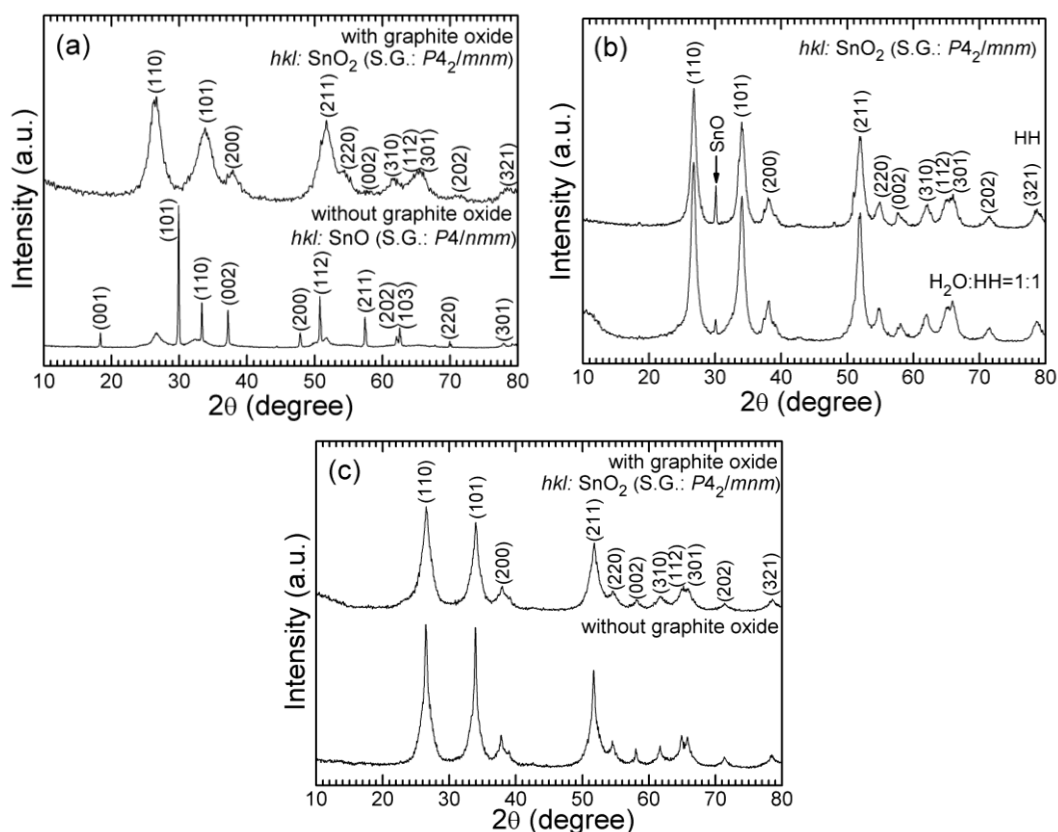

Figure 1. XRD patterns of the hydrothermal products at 180 °C for 4 h using Sn^{2+} as the precursor (a) in DI water, (b) in HH and H$_2$O/HH, and (c) using Sn^{4+} as the precursor in DI water.

Fig. 2(a) displays the SEM images of SnO$_2$/G. It is obvious from the transparent graphene that nanosized SnO$_2$ particles are loaded between the graphene sheets. TEM images indicate that the SnO$_2$ nanoparticles are uniformly dispersed by the graphene as seen in Fig. 2(b). We can observe both dark regions with densely scattered particles and light regions with sparsely scattered particles in Fig. 2(b). Fig. 2(c) presents the enlarged view of a dark region in Fig. 2(b). Obviously, the dark region is composed of multi-layered graphene with SnO$_2$ nanoparticles attached on each layer. As seen in Fig. 2(d), the SnO$_2$ nanoparticles exhibit a rather small size of below 10 nm, in agreement with the broad diffraction peaks in Fig. 1(a). The HRTEM image also indicates that the SnO$_2$ is well crystallized even though prepared at a low temperature. It should be stressed that the attached nanosized SnO$_2$, on the other hand, also prevents the graphene sheets from aggregating. The absence of the (002) peak of graphene supports this assumption.

Fig. 3(a) shows the SEM images of SnO prepared by the hydrothermal route without adding the graphite oxide. In this case, Sn^{2+} directly hydrolyzes to form flake-like SnO. Note that the SnO flakes with a size of around 100 nm aggregate into large-sized bulks. The SnO$_2$ nanoparticles also tend to aggregate without the dispersion of graphene as shown in Fig. 3(b). In contrast to the case in SnO$_2$/G,

the SnO$_2$ nanoparticles are not homogeneously dispersed by the graphene in SnO$_2$/G2 (Fig. 3(c)), due possibly to the rapid, direct hydrolysis of Sn^{4+} into SnO$_2$ before the reduction of the graphite oxide. For SnO$_2$/G, the interaction between the graphite oxide and Sn^{2+} may be responsible for the uniform dispersion of SnO$_2$ nanoparticles on graphene.
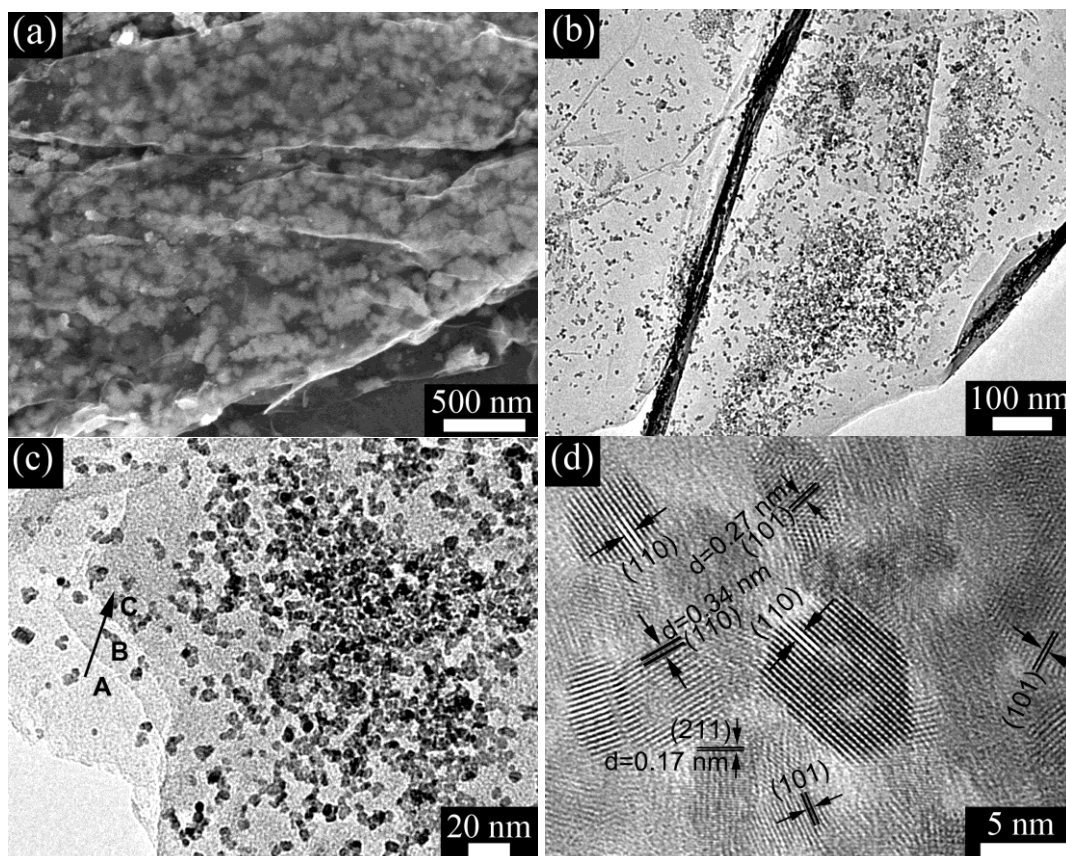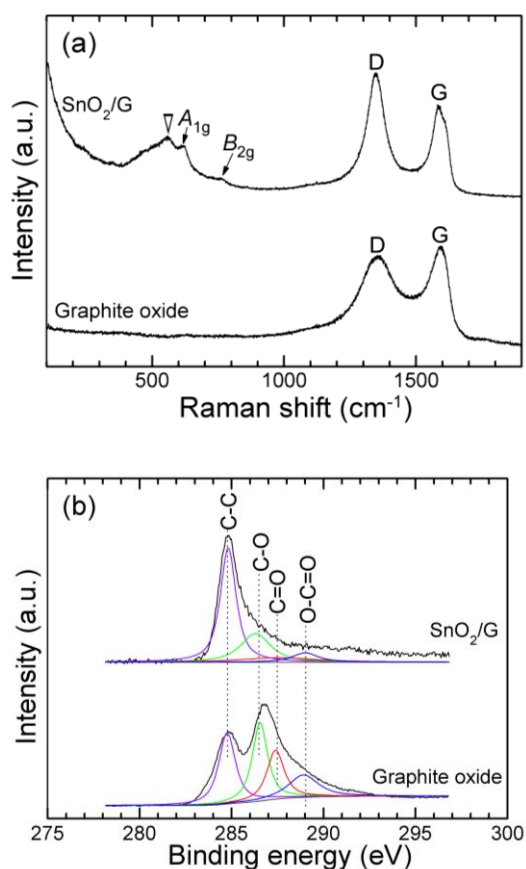

Figure 2. Morphologies of SnO$_2$/G: (a) SEM, (b) low-magnification TEM, (c) high-magnification TEM, and (d) HRTEM images.
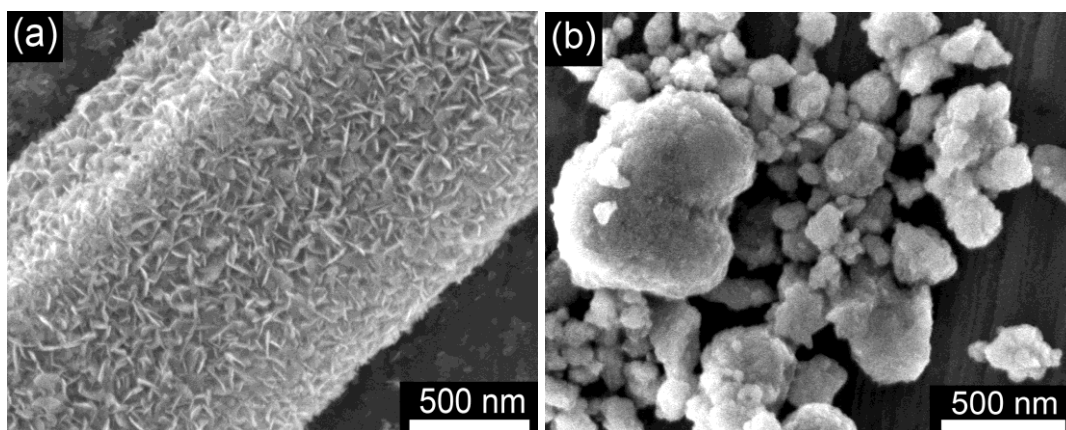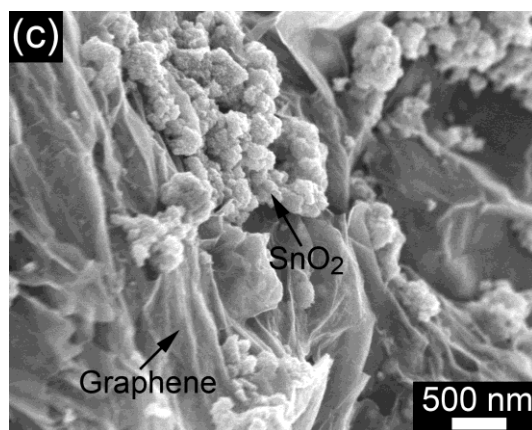
Figure 3. SEM images of (a) SnO, (b) SnO_2, and (c) SnO_2/G2.

The formation and growth of SnO_2 are retarded because Sn^{2+} should be oxidized to Sn^{4+} first. It is likely that the reduction of the graphite oxide and the formation of SnO_2 take place simultaneity.


Figure 4. Raman spectra (a) and C 1s XPS (b) of SnO_2/G and the graphite oxide.

To check whether the graphite oxide was reduced to graphene, Raman spectra and XPS measurements were conducted. Fig. 4(a) compares the Raman spectra of the graphite oxide and

SnO$_2$/G. Two Raman bands at 1350 and 1580 cm^{-1} appear for both the samples which correspond to the disordered (D) and graphitic (G) bands, respectively, of carbon materials [29]. Compared to the graphite oxide, SnO$_2$/G exhibits an increased D/G intensity ratio which is caused by a decreased average size of the sp^2 domains and an increased number of these domains, signifying the conversion from graphite oxide to graphene [30]. The bands at around 630 and 770 cm^{-1} are related to the A_{1g} and B_{2g} vibration modes, respectively, of SnO$_2$ [31]. The band at about 570 cm^{-1} (denoted by the hollow triangle) corresponds to the in-plane oxygen vacancy at the SnO$_2$ nanocrystal surface [32].

Fig. 4(b) compares the C1s XPS spectra of the graphite oxide and SnO$_2$/G. For the graphite oxide, the carbon in C-O bonds (286.3 eV), carbonyl carbon (C=O, 287.6 eV) and carboxylate carbon (O-C=O, 289. 0 eV) all exhibit a high intensity, indicating considerable oxidation of graphite [30, 33, 34]. For SnO$_2$/G, the relative intensity of the sp^2 carbon (C-C, 284.8 eV) and oxygen-bonded carbon shows a significant increase, suggesting a sufficient reduction of graphite oxide to graphene, in consistent with the Raman results.
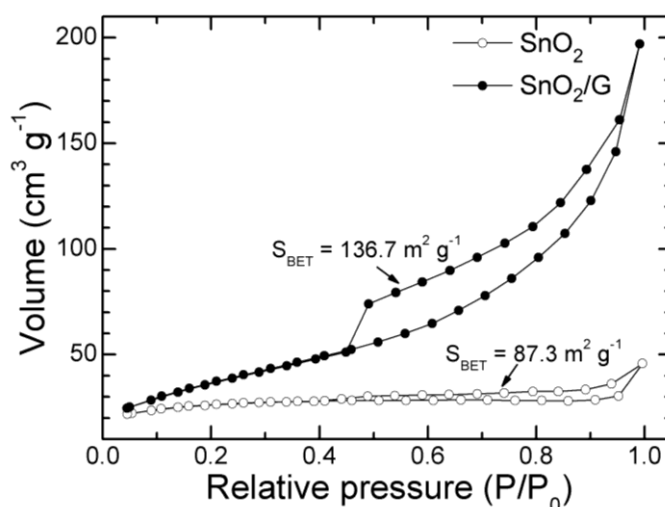

Figure 5. Nitrogen adsorption/desorption isotherms of SnO$_2$/G and SnO$_2$.

Fig. 5 demonstrates nitrogen adsorption/desorption isotherms of SnO$_2$/G and SnO$_2$. From the figure, the Brunauer-Emmett-Teller (BET) specific surface area can be derived. As expected, the SnO$_2$/G sample exhibits a much higher BET specific surface area (S_{BET}) than bare SnO$_2$, because of the restrained aggregation of the SnO$_2$ nanoparticles and the introduction of graphene with a large S_{BET}. The graphene content in SnO$_2$/G was measured to be 16% wt by the TGA result. The relatively low content of graphene means that the obvious increase in S_{BET} should be ascribed mainly to the hybrid nanostructure that is the SnO$_2$ nanoparticles are uniformly dispersed and confined by the graphene sheets.

Fig. 6(a) shows the charge (Li-extraction) and discharge (Li-insertion) curves of SnO$_2$/G at a current density of 50 mA g^{-1}. This sample yields first discharge and charge capacities of 1662 and 762 mAh g^{-1}, respectively. A quasi-plateau appears at 0.5–1.0 V during the first discharge process. The

quasi-plateau is related to the irreversible formation of Li_2O and the solid electrolyte interface (SEI) layer. Note that the first charge capacity of SnO_2/G is close to the theoretical value of SnO_2 (780 mAh g^{-1}), indicative of a sufficient utilization of the active material.
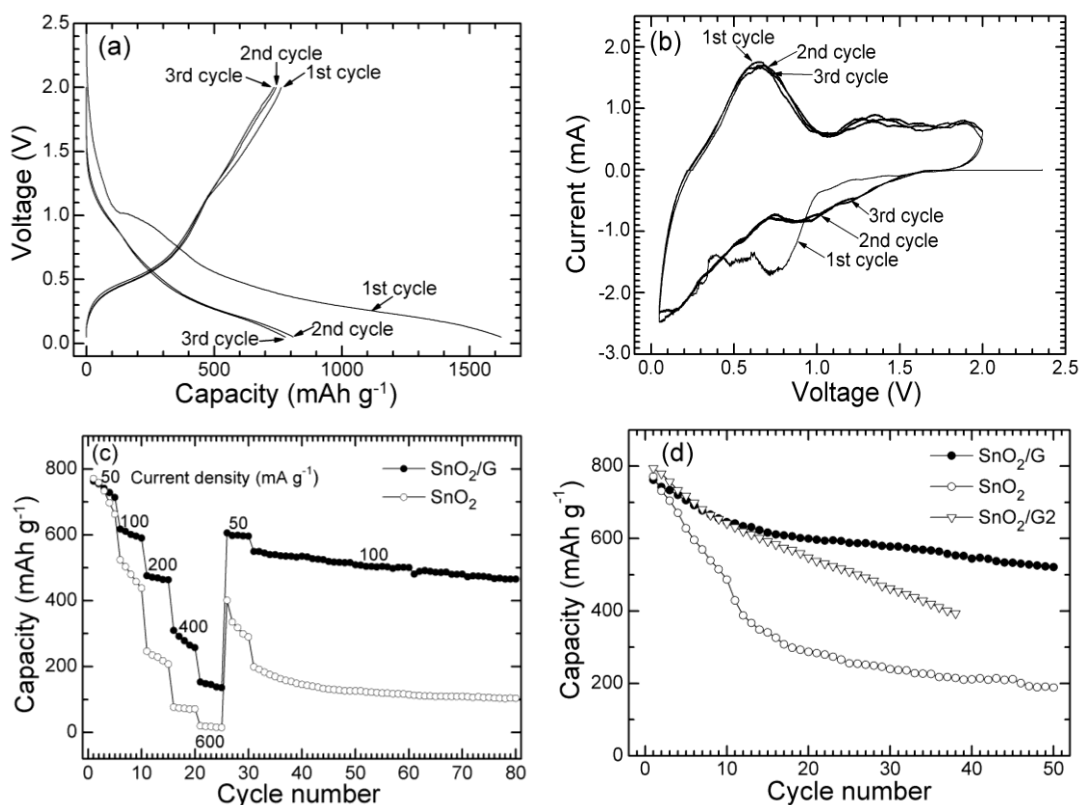

Figure 6. Charge-discharge curves at 50 mA g^{-1} (a) and CV plots at 0.1 mV s^{-1} (b) of SnO_2/G, (c) comparison of rate capability between SnO_2/G and SnO_2, and (d) comparison of cycling stability among SnO_2/G, $SnO_2/G2$ and SnO_2 at 50 mA g^{-1}.

The CV plots scanned at 0.1 mV s^{-1} are shown in Fig. 6(b). The reduction peak at 0.5−1.0 V in the first scan corresponds to the quasi-plateau in the first discharge curve. After the first cycle, reversible electrochemical reactions occur evidenced by the almost overlapped reduction peaks (0−0.4 V) and oxidation peaks (0.5−1.0 V).

The rate capability of SnO_2/G and bare SnO_2 is compared in Fig. 6(c). SnO_2/G shows an obviously improved rate capability compared with bare SnO_2. The enhancement in rate capability is due to the following factors: first, the highly conducting graphene supplies a two-dimensional conducting network for the SnO_2 nanoparticles; second, the well-dispersed, small-sized SnO_2 is favorable for rapid Li-ion diffusion; third, the larger specific surface area of SnO_2/G is beneficial for a better wetting of the active material by the electrolyte, thus decreasing the charge transfer resistance between the active material and the electrolyte. Note that the charge capacity can be well recovered when the current is switched from a high to a low value for SnO_2/G, indicating a good reversibility of the electrode. In addition, SnO_2/G also exhibits a good cycling stability at 100 mA g^{-1}. The bare SnO_2

electrode, on the contrary, demonstrates an inferior ability to recover capacity when the current is shifted to the low value.
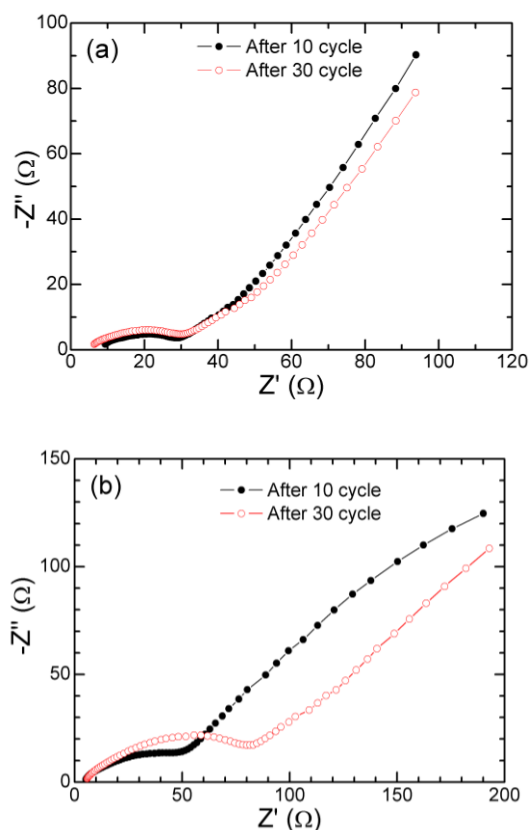
Figure 7. Nyquist plots of (a) SnO_2/G and (b) SnO_2 after 10 and 30 cycles.

Fig. 6(d) compares the cycling stability among SnO_2/G, $SnO_2/G2$ and bare SnO_2. Clearly, SnO_2/G displays an enhanced cycling stability compared with bare SnO_2 especially in the initial 10 cycles. After 50 cycles at 50 mA g^{-1}, SnO_2/G still maintains a charge capacity over 500 mAh g^{-1}, while bare SnO_2 only gives a charge capacity below 200 mAh g^{-1}. The improved cycling stability can be attributed to the introduction of graphene which not only buffers the large volume changes upon Li-insertion/extraction because of its good flexibility and large mechanical strength, but also prevents the particles from aggregating due to its effective confining effect. SnO_2/G also exhibits a better cycling stability than $SnO_2/G2$ even though they were prepared by a similar procedure. The small size and homogeneous dispersion of the SnO_2 particles for SnO_2/G are considered to be responsible for its better cycling stability. For $SnO_2/G2$, however, local aggregation occurs for both the SnO_2 particles and the graphene sheets. In this regard, it seems that Sn^{2+} is more suitable to be used as the tin source to synthesize SnO_2-graphene nanocomposite.

To understand different electrochemical behaviors between SnO_2/G and bare SnO_2, EIS measurements were carried out as indicated in Fig. 7. The Nyquist plots were recorded after the electrodes have been cycled for 10 and 30 times. The plots consist of a depressed semicircle in the high-to-medium frequency region and a slopping line in the low frequency region. As previously

reported [35], the semicircle corresponds to the charge transfer resistance (R_{ct}) and the slopping line is related to the Li-ion diffusion in the bulk material. As seen in Fig. 7(a), R_{ct} keeps almost unchanged after 10 and 30 cycles for SnO_2/G, which means that the electrode exhibits a stable charge transfer reaction, implying a good electrochemical stability. In contrast, the bare SnO_2 demonstrates a large increase in R_{ct}, suggesting that the charge transfer reaction becomes sluggish upon repeated cycling. As a result, the EIS tests agree well with difference in the electrochemical properties between SnO_2/G and bare SnO_2.

4. CONCLUSIONS

SnO_2-graphene nanocomposite has been synthesized by a simple one-pot solvothermal route. The SnO_2 nanoparticles with a size below 10 nm are uniformly loaded on the graphene sheets when using Sn^{2+} as the precursor. The interaction between the graphite oxide and Sn^{2+} is responsible for the small size and the homogeneous dispersion of the SnO_2 nanoparticles. The SnO_2-graphene nanocomposite exhibits improved electrochemical properties compared to bare SnO_2 due to the incorporation of graphene which acts both as a buffer to alleviate the volume changes and as a separator to refrain the aggregating of the particles. Furthermore, the introduced graphene offers a conducting channel for SnO_2 and increases the specific surface area, enhancing the electrode reaction kinetics. Compared with SnO_2/G2 using Sn^{4+} as the precursor, SnO_2/G using Sn^{2+} as the precursor shows better electrochemical properties due to more homogeneous dispersion and smaller size of the SnO_2 nanoparticles. The good electrochemical properties of SnO_2/G make it a promising anode material for Li-ion batteries.

References

1. Y. Idota, T. Kubota, A. Matsufuji, Y. Maekawa, and T. Miyasaka, *Science* 276 (1997) 1395.
2. I.A. Courtney and J. R. Dahn, *J. Electrochem. Soc.* 144 (1997) 2045.
3. J. Y. Huang, L. Zhong, C. M. Wang, J. P. Sullivan, W. Xu, L. Q. Zhang, S. X. Mao, N. S. Hudak, X. H. Liu, A. Subramanian, H. Y. Fan, L. Qi, A. Kushima, and J. Li, *Science* 330 (2010) 1515.
4. C. M. Wang, W. Xu, J. Liu, J. G. Zhang, L. V. Saraf, B. W. Arey, D. Choi, Z. G. Yang, J. Xiao, S. Thevuthasan, and D. R. Baer, *Nano Lett.* 11 (2011) 1874.
5. C. Kim, M. Noh, M. Choi, J. Cho, and B. Park, *Chem. Mater.* 17 (2005) 3297.

6. X. W. Lou, D. Deng, J. Y. Lee, and L. A. Archer, *Chem. Mater.* 20 (2008) 6562.
7. X. W. Lou, J. S. Chen, P. Chen, and L. A. Archer, *Chem. Mater.* 21 (2009) 2868.
8. K. E. Aifantis, S. Brutti, S. A. Hackney, T. Sarakonsri, and B. Scrosati, *Electrochim. Acta* 55(2010) 5071.
9. Y. S. Lin, J. G. Duh, and M. H. Hung, *J. Phys. Chem. C* 114 (2010) 13136.
10. Y. Wang and J. Y. Lee, *Electrochem. Commun.* 5 (2003) 292.
11. Y. Wang, J. Y. Lee, and B. H. Chen, *J. Electrochem. Soc.* 151 (2004) A563.
12. J. G. Kim, S. H. Nam, S. H. Lee, S. M. Choi, and W. B. Kim, *ACS Appl. Mater. Interfaces* 3 (2001) 828.
13. C. H. Xu, J. Sun, and L. Gao, *J. Phys. Chem. C* 113 (2009) 20509.
14. P. Wu, N. Du, H. Zhang, J. X. Yu, and D. R. Yang, *J. Phys. Chem. C* 114 (2010) 22535.
15. A.Dhanabalan, Y. Yu, X. F. Li, W. Chen, K. Bechtold, L. Gu, and C. L. Wang, *J. Mater. Res.* 25 (2010) 1554.
16. K. S. Novoselov, A. K. Geim, S. V. Morozov, D. Jiang, Y. Zhang, S. V. Dubonos, I. V. Grigorieva, and A. A. Firsov, *Science* 306 (2004) 666.
17. M. D. Stoller, S. Park, Y. W. Zhu, J. H. An, and R. S. Ruoff, *Nano Lett.* 8 (2008) 3498.
18. S. Park, J. H. An, I. W. Jung, R. D. Piner, S. J. An, X. S. Li, A. Velamakanni, and R. S. Ruoff, *Nano Lett.* 9 (2009) 1593.
19. C. Lee, X. D. Wei, J. W. Kysar, and J. Hone, *Science* 321 (2008) 385.
20. S. M. Paek, E. Yoo, and I. Honma, *Nano Lett.* 9 (2009) 72.
21. J. Yao, X. P. Shen, B. Wang, H. K. Liu, and G. X. Wang, *Electrochem. Commun.* 11 (2009) 1849.
22. L. S. Zhang, L. Y. Jiang, H. J. Yan, W. D. Wang, W. Wang, W. G. Song, Y. G. Guo, and L. J. Wan, *J. Mater. Chem.* 20 (2010) 5462.
23. Y. M. Li, X. J. Lv, J. Lu, and J. H. Li, *J. Phys. Chem. C* 114 (2010) 21770.
24. D. H. Wang, R. Kou, D. W. Choi, Z. G. Yang, Z. M. Nie, J. Li, L. V. Saraf, D. H. Hu, J. G. Zhang, G. L. Graff, J. Liu, M. A. Pope, and I. A. Aksay, *ACS Nano* 4 (2010) 1587.
25. X. Y. Wang, X. F. Zhou, K. Yao, J. G. Zhang, and Z. P. Liu, *Carbon* 49 (2011) 133.
26. W. S. Hummers and R. E. Offeman, *J. Am. Chem. Soc.* 80 (1958) 1339.
27. X. F. Gao, J. Jang, and S. Nagase, *J. Phys. Chem. C* 114 (2010) 832.
28. Z. H. Han, N. Guo, F. Q. Li, W. Q. Zhang, H. Q. Zhao, and Y. T. Qian, *Mater. Lett.* 48 (2001) 99.
29. F. Tuinstra and J. L. Koenig, *J. Chem. Phys.* 53 (1970) 1126.
30. S. Stankovich, D. A. Dikin, R. D. Piner, K. A. Kohlhaas, A. Kleinhammes, Y. Y. Jia, Y. Wu, S. T. Nguyen, and R. S. Ruoff, *Carbon* 45 (2007) 1558.
31. K. N. Yu, Y. H. Xiong, Y. L. Liu, and C. S. Xiong, *Phys. Rev. B* 55 (1997) 2666.
32. L. Z. Liu, X. L. Wu, F. Gao, J. C. Shen, T. H. Li, and P. K. Chu, *Solid State Commun.* 151 (2011) 811.
33. S. Stankovich, R. D. Piner, X. Q. Chen, N. Q. Wu, S. T. Nguyen, and R. S. Ruoff, *J. Mater. Chem.* 16 (2006) 155.
34. L. Zhang, Y. Li, L. Zhang, D. W. Li, D. Karpuzov, Y. T. Long, *Int. J. Electrochem. Sci.* 6 (2011) 819.
35. H. Li, X. J. Huang, and L. Q. Chen, *J. Power Sources* 81−82 (1999) 340.